Li *et al. Chin. J. Mech. Eng.* (2019) 32:85
https://doi.org/10.1186/s10033-019-0402-2

Chinese Journal of Mechanical Engineering

ORIGINAL ARTICLE Open Access

Effect of RANS Turbulence Model on Aerodynamic Behavior of Trains in Crosswind

Tian Li*, Deng Qin and Jiye Zhang

Abstract

The numerical simulation based on Reynolds time-averaged equation is one of the approved methods to evaluate the aerodynamic performance of trains in crosswind. However, there are several turbulence models, trains may present different aerodynamic performances in crosswind using different turbulence models. In order to select the most suitable turbulence model, the inter-city express 2 (ICE2) model is chosen as a research object, 6 different turbulence models are used to simulate the flow characteristics, surface pressure and aerodynamic forces of the train in crosswind, respectively. 6 turbulence models are the standard *k-ε*, Renormalization Group (RNG) *k-ε*, Realizable *k-ε*, Shear Stress Transport (SST) *k-ω*, standard *k-ω* and Spalart–Allmaras (SPA), respectively. The numerical results and the wind tunnel experimental data are compared. The results show that the most accurate model for predicting the surface pressure of the train is SST *k-ω*, followed by Realizable *k-ε*. Compared with the experimental result, the error of the side force coefficient obtained by SST *k-ω* and Realizable *k-ε* turbulence model is less than 1 %. The most accurate prediction for the lift force coefficient is achieved by SST *k-ω*, followed by RNG *k-ε*. By comparing 6 different turbulence models, the SST *k-ω* model is most suitable for the numerical simulation of the aerodynamic behavior of trains in crosswind.

Keywords: Turbulence model, Crosswind, High speed train, Numerical simulation, Aerodynamic

1 Introduction

The aerodynamic characteristics of a high-speed train have an important impact on its economy, stability, and safety. Especially in the case of crosswind, the aerodynamic force changes significantly due to the variation of the flow field, and the train may be in a high-risk state of derailment and overturning [1–5]. Therefore, it is very important to study the aerodynamic characteristics of high-speed trains in crosswind. In the aerodynamics standards of the railway industry and the European railway application aerodynamics standard, the numerical simulation based on Reynolds-averaged Navier–Stokes (RANS) equation is one of the approved methods to evaluate the aerodynamic performance of trains in crosswind. Up to now, many researchers have conducted numerical studies on the operation of high-speed trains in crosswind conditions [6–10]. Li et al. [11] investigated a numerical simulation method for the interaction between airflow and high-speed trains, indicating that it is necessary to consider the interaction between airflow and a high-speed train subjected to crosswind. Yu et al. [12] selected the aerodynamic drag force and wheel unloading rate as the optimization targets, and proposed a multi-objective shape optimization design method for high-speed train head. In computational fluid dynamics (CFD), the selection of the turbulence model is critical. The numerical results obtained by different turbulence models may be different, and the assumed turbulence model will be different according to the research object and flow characteristics.

The choice of turbulence models was different in the application of the numerical simulation of train flow fields. In previous studies, few have fully studied the influence of the turbulence model on the flow field around the train. Different turbulence models were chosen. For RANS, the standard *k-ε* and Realizable *k-ε* turbulence model were used to predict the aerodynamics of the vehicles [13, 14]. It has been verified that the SST *k-ω* turbulence model can

*Correspondence: litian2008@home.swjtu.edu.cn
State Key Laboratory of Traction Power, Southwest Jiaotong University, Chengdu 610031, China

better predict the aerodynamic forces and pressure on the train surface [15–17]. Large eddy simulation (LES) and detached eddy simulation (DES) method were also used to study the aerodynamic performances of trains [18–22]. The choice of the turbulence model plays a critical role in the calculation accuracy of the numerical simulation. Some researchers have conducted studies on the accuracy of different turbulence models for different research objects. As indicated in Fu et al. [23], the different turbulence models show different numerical simulation performances for a full-scale car. If considering the unsteady characteristics of the air flow, selecting the appropriate RANS turbulence model based on the flow characteristics can improve the accuracy of the unsteady simulation and reduce the calculation time [24]. When high-speed trains run at a high speed, different turbulence models have great differences in the simulation accuracy of the flow field around them. Wang et al. [25] investigates and evaluates the performance of three widely used turbulence models including the unsteady RANS, Scale-Adaptive Simulation (SAS) and DES to predict the slipstream of a generic train. Munoz-Paniagua et al. [26] analyzed the aerodynamic force coefficients of and pressure distribution on the train surface, the time average and instantaneous flow structures. The effect of SAS and improved delayed detached eddy simulation turbulence models on the aerodynamic characteristics of a train in crosswind was studied.

In the case of crosswind, the flow characteristics of the train vary greatly. The extent and mechanism of the influence of the turbulence model on the aerodynamic performance of trains have not been studied comprehensively, therefore, most researchers choose the turbulence model based on experience. In this study, the ICE2 model is chosen as a research object, and 6 common RANS turbulence models are used to numerically simulate the train surface pressure, flow characteristics and aerodynamic performance under crosswind. By comparing the numerical simulation results with the experimental data obtained by the wind tunnel experiments, the most suitable turbulence model for simulating the train flow around crosswind is studied.

2 Governing Equations

2.1 Navier–Stokes Equations

The motion of the airflow around trains can be described by a continuity equation, a momentum equation, and an energy equation. The general governing equations are as follows:

$$\frac{\partial(\rho\boldsymbol{\Phi})}{\partial t} + div(\rho \boldsymbol{V}\boldsymbol{\Phi}) = div(\boldsymbol{\Gamma} grad\boldsymbol{\Phi}) + \boldsymbol{S}, \tag{1}$$

where ρ is the density, t is the time variable, $\boldsymbol{\Phi}$ is a general variable, which can represent u, v, w, T, and the others, $\boldsymbol{V}$ is the velocity vector, $\boldsymbol{\Gamma}$ is the general diffusion coefficient, $\boldsymbol{S}$ is the generalized source term. The left side of the equation is the transient term and the convection term, and the right side of the equation is the diffusion term and the source term.

2.2 Turbulence Model

When a train runs at a high speed, the flow around the train can be treated as a three-dimensional incompressible flow process. A reasonable turbulent transport equation must be selected for the numerical simulation. The RANS simulation is currently the most widely used turbulent numerical method. The Reynolds stress term in the RANS equation is unknown, resulting in the unclosed equations. The eddy viscosity model introduces the turbulent viscosity μ_t based on the Boussinesq hypothesis and establishes the relationship of Reynolds stress with respect to the average velocity gradient. According to the number of differential equations that determine the turbulent viscosity μ_t, the eddy viscosity model is divided into zero-equation model, one-equation model, and two-equation model [27]. The one-equation model is mainly Spalart–Allmaras. Typical two-equation models include the standard k-ε, RNG k-ε, Realizable k-ε, SST k-ω, and standard k-ω. In this paper, the one-equation and 5 two-equation models commonly used in engineering are selected for comparison. The standard k-ε, RNG k-ε, Realizable k-ε, SST k-ω, standard k-ω, and Spalart–Allmaras turbulence models are respectively represented by SKE, RNG, RKE, SST, SKW, and SPA for simplicity.

2.3 Wall Function

Whether it is the standard k-ε model, RNG k-ε model or Realizable k-ε model, it is effective for fully developed turbulent flows, that is, these models are high Reynolds turbulence models, and they can only be used to solve the flow fully developed. In the near-wall region, the turbulent flow is not fully developed. In the region closer to the wall, the flow may be in a laminar flow state. Therefore, it is difficult to use the previous high Reynolds model for the calculation in the near-wall region, and special processing should be used. A wall function method or a k-ε model with a low Re number can be used. The wall function method is actually a set of semi-empirical formulas used to directly relate the physical quantities on the wall to the unknowns, in conjunction with the high Re number k-ε model. A standard wall function is used when the dimensionless wall distance $y+$ is in the range of 30 and 200, and a reinforced wall function is used when $y+$ is close to 1. For the k-ω turbulence model, $y+$ is guaranteed to be close to 1.

3 Numerical Information

3.1 Train Model

The model is an ICE2 train, as shown in Figure 1(a), which consists of a head car and a part of the tail car. The tail car is mainly used to ensure the flow field of the head car and between the head and tail cars. There is a 5 mm gap to ensure the separate measurement of the head and tail forces. The numerical simulation calculation model is consistent with the wind tunnel test model [28]. The scale size of the train model is 1:10, the total length of the scaled train $L=3.552$ m, the width $B=0.302$ m, the height $H=0.358$ m, and the streamlined length $L_{\text{head}}=2.656$ m, the incoming flow is shown in Figure 1(b). Taking the center of the section as the origin, it is divided into four parts according to the angle, as shown in Figure 1(b). 4 parts are the upper surface (0°–45°, 315°–360°), leeward surface (45°–135°), bottom surface (135°–225°) and windward surface (225°–315°). Figure 2 illustrates the speed vector diagram, where U_t is the train's running speed; U_w is the crosswind velocity; U_R is the air speed relative to the train; β is the yaw angle. The experimental data were obtained from the Bombardier Transportation Company of the Zhukovsky Central Aerodynamics Institute in Russia in 2003 in the T-103 open-air jet tunnel [28].

3.2 Numerical Method

The size of the computational domain should satisfy the requirement that it will not affect the flow field around the train. The computational domain shown in Figure 3 is established. The gap between the train and ground is 0.0503 m, and the length, width, and height of the computational domain are 16 m, 12 m and 4 m, respectively. The entrance plane in front of the train is 4 m from the nose of the head car, and the distance between the center line of the train and the left and right sides is 4 m and 8 m, respectively.

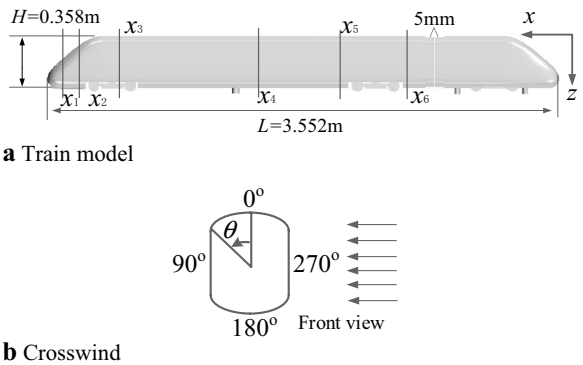

Figure 1 Model geometry

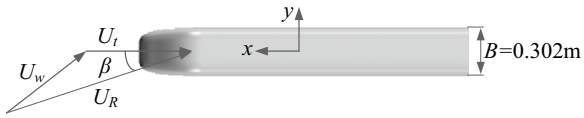

Figure 2 Air speed relative to the train

The boundary conditions are set as follows: the two entrances of the computational domain are specified as the inlet boundary conditions with a speed of 60.62 m/s and the crosswind velocity of 35 m/s. The two exits are set as the pressure outlets, and the ground and train surfaces are fixed wall boundaries. The top surface of the computational domain is symmetry, as shown in Figure 3. The air density is 1.205 kg/m^3 and the kinematic viscosity is 1.81×10^{-5} Pa·s. The SIMPLE algorithm of pressure-velocity coupling is used, and the second-order scheme is chosen for the discretization for all variables.

The pressure coefficient c_p, aerodynamic side force coefficient c_s and lift force coefficient c_l are defined as:

$$c_p = \frac{p - p_\infty}{0.5\rho u_\infty^2}, \tag{2}$$

$$c_s = \frac{F_s}{0.5\rho u_\infty^2 A}, \tag{3}$$

$$c_l = \frac{F_l}{0.5\rho u_\infty^2 A}, \tag{4}$$

where p is the static pressure, p_∞ is the reference pressure, ρ is the air density; u_∞ is the incoming flow velocity, F_s and F_l are the aerodynamic side and lift forces, respectively; A is the characterized area of the train.

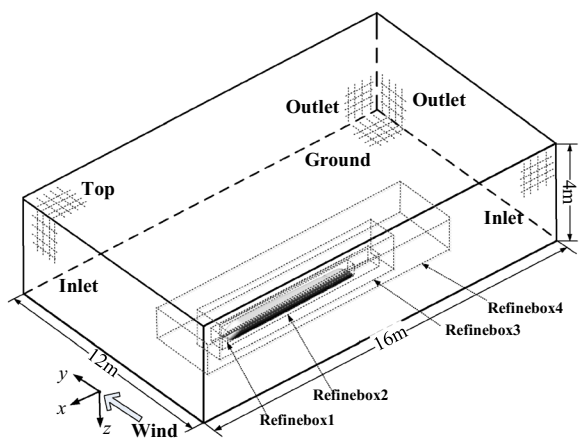

Figure 3 Computational domain

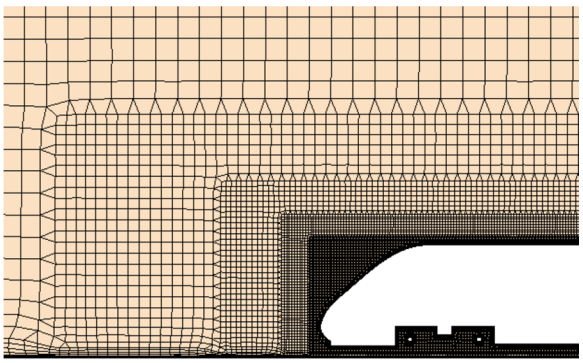

Figure 4 Grid at the cross-section $y=0$ m

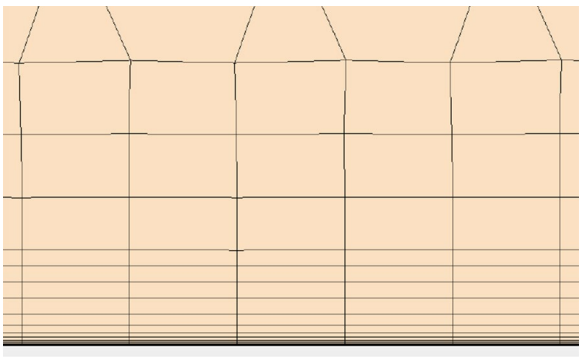

Figure 5 Boundary layer grid

3.3 Computational Mesh

In order to simulate the flow around the train better, the flow field is multi-layered and refined. The grid size is gradually increased to ensure a fine grid. The refined region is shown in Figure 4. Since the fluid variable in the near wall region has a large gradient, a fine mesh near wall region can basically determine the true physical phenomenon of the rear wall. A boundary layer is created on the surface of the train to simulate the flow near the wall. The first layer of the boundary layer has a height of 0.01 mm, a growth rate of 1.2. There are 12 layers in total, ensuring that $y+$ is close to 1. After selecting the reasonable mesh size for meshing, the mesh of the flow field around the train model is shown in Figure 4. The mesh in the boundary layer of the train surface is shown in Figure 5.

The accuracy of the numerical results is related to the number and quality of the mesh, therefore, the mesh independence is studied firstly. Three sets of grids were divided by changing the size of the train components. The SST k-ω turbulence model is used for the numerical calculation. The side force coefficients c_s obtained using different grids are shown in Table 1. The relative error of the side force coefficients is within 3%. When the number of meshes increases from 23.81 million to 29.85 million, the relative error in the side force coefficient is less than 2%. It can be seen that the further increase of the mesh has little effect on the side force coefficient, therefore, the grid with a number of 23.81 million is chosen for the remaining numerical calculations.

Table 1 Grid independence study results

Mesh	Surface size (mm)	Number of grids (million)	c_s	Relative error (%)
1	112	11.95	4.09	–
2	80	23.81	4.00	−2.20
3	72	29.85	4.04	1.22

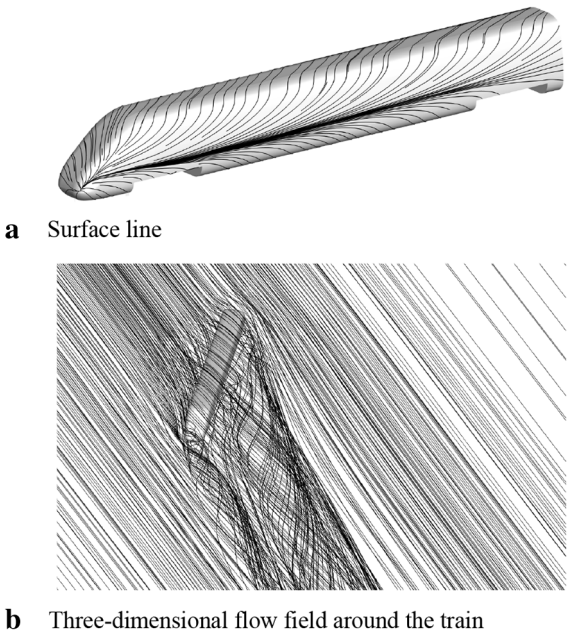

a Surface line

b Three-dimensional flow field around the train

Figure 6 Flow structure

4 Results

The numerical simulations were carried out with 6 turbulence models, which are SKE, RNG, RKE, SKW, SST and SPA, and the flow characteristics of ICE2 train in crosswind are analyzed.

4.1 Flow Distribution

When the train is running in a crosswind environment, its surrounding flow field is shown in Figure 6. When the airflow is blocked by the train, it is divided into two parts sourced from the windward side of the train, a part of the airflow bypasses the roof and the other flows from the bottom of the train (see Figure 6(a)). A large number of

eddies are formed on the leeward side of the train, and the flow field is extremely complicated (see Figure 6(b)).

Figure 7 shows the streamlines at different cross-sections of the train using SST *k-ω* turbulence model. The corresponding cross-sectional location is shown in Figure 1(a). When the steady airflow under certain conditions bypasses the train, a vortex is formed from the surface, that is, the boundary layer is detached, and the airflow over the roof and bottom is collected on the leeward side of the train, generating a lot of vortices. At different cross-sections, the number and scale size of vortices are different. When the air flows over the roof and the bottom of the vehicle, the shedding eddy is likely to occur on the leeward side of the train. It can be seen from different sections that as the airflow develops downstream, the scale of the vortex shedding becomes larger and larger, and the vortices are gradually far from the vehicle body. There are many large-scale vortices on the leeward side of the train. These vortices consume energy and generate a large suction pressure on the leeward side of the train.

The surrounding flow field obtained using different turbulence models are shown in Figure 8. Due to the similarity, only the flow field distribution at the cross-section $x_5 = -2.06$ m is given. Different turbulence models have different simulation capabilities for the flow field. As shown in Figure 8(e), the SST *k-ω* turbulence model captures four typical vortices, defined as V_{c1}, V_{c2}, V_{c3}, and V_{c4}, respectively. Three turbulence models including RNG, SKW and SST have the ability to capture the above vortices. The other three turbulence models do not capture the V_{c1} vortex, and the SKE turbulence model also has poor recognition of several other vortices. The V_{c3} vortex is not obtained using RNG turbulence model, and the V_{c3} and V_{c4} vortices identified by SKW turbulence model are interconnected.

In order to further analyze the flow field, Figure 9 shows the comparison of the velocity distributions at different cross-sections. When the airflow is blocked by the train, the flow velocity is significantly reduced, and the airflow speed increases significantly when the airflow bypasses the roof and the vehicle bottom. As there are many vortex structures on the leeward side of the train, the flow velocity in the above regions is relatively low. Obviously, the calculation results show that the velocity distribution obtained using different turbulence models are different. The SKE turbulence model performs poorly compared with the other turbulence models. The other turbulence models show higher gradients in velocity. 4 turbulence models including RNG, SKW, SST and SPA show a lower velocity near the leeward side of the train, and RNG and SST turbulence models present a higher resolution of the velocity gradient.

4.2 Train Surface Flow

Figures 10 and 11 show the flow pattern on the train surface including the leeward side and the bottom. The airflow branches off from the windward surface of the train,

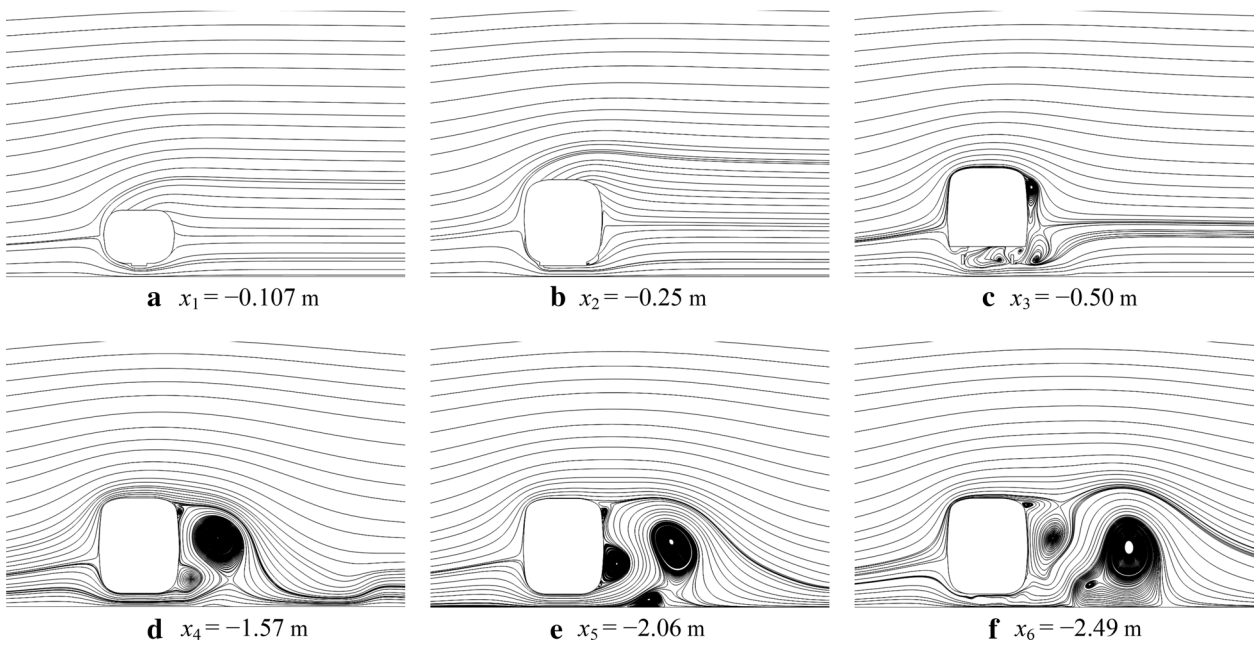

Figure 7 Streamline at different cross-sections for SST

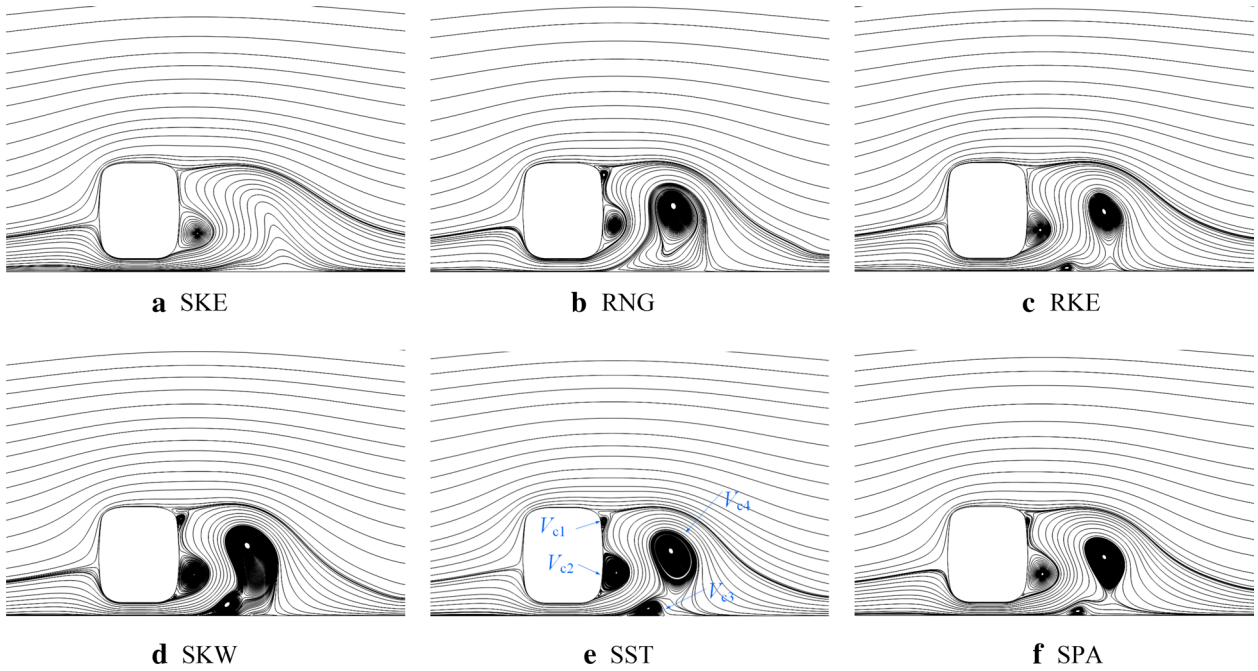

Figure 8 Streamline at the cross-section $x_5 = -2.06$ m with different turbulence model

some flows over the roof and the others over the bottom of the train, as shown in Figure 6(a). There are many separation lines (red) and reattachment lines (black) on the surface of the train, mainly including separation lines S1, S2, S3 and reattachment lines A1, A2, A3, as shown in Figure 10(e). For the upper surface, airflow is separated at the separation line S1, and reattached at the reattachment line A2, and then separated again from the separation line S3. The airflow adheres to the surface of the train body at the reattachment line A2, and then separates at the separation line S3, and reattaches again at the reattachment line A1, and the airflow flows downstream to the separation line S1. The underneath airflow is separated at the separation line S2 and reattached at the reattachment line A3. The flow pattern around the bogie is more complicated, and the airflow has multiple separation and reattachment lines. The separation and reattachment of the airflow at the front end of the train will form bubbles. The air bubbles will fall off and develop to the downstream along the train. Once the air bubbles fall off, new air bubbles will be generated. When these air bubbles flow backward, the airflow on the leeward side of the train will be intensified, forming a large vortex.

The simulation results of the separation lines (S1 and S3) and the reattachment line (A1) for SKE and RKE are poor. RNG and SPA turbulence models predict a higher position of the separation line S3, and RNG turbulence model also has a higher predicted position for the reattachment line A2. However, the SPA turbulence model has a lower predicted position for the reattachment line A2. The three turbulence models including RKE, SKW and SST have similar predictions for the reattachment line A2. The length of the separation line S3 predicted using SKW turbulence model is significantly larger than the other models. The position and length of these surface flow lines represent the position and the size of the region for the airflow varied from the two-dimensional surface to the three-dimensional flow field. Obviously, different turbulence models have different predictions in surface flow.

4.3 Pressure Distribution

Figure 12 shows the pressure distribution around the train at the cross-section $x_4 = -1.57$ m. From the previous flow field analysis, it is only obvious that the results obtained using different turbulence models are different. 3 turbulence models including RNG k-ε, standard k-ω and SST k-ω show lower negative pressure on the leeward surface of the train, and the pressure gradient on the leeward surface is larger, while the other three turbulence models show a higher negative pressure, and a smaller pressure gradient.

Figure 13 shows the comparison of the surface pressure coefficient c_p and the experimental ones on different cross-sections of the train. The pressure coefficient on the windward surface and the top surface of the train

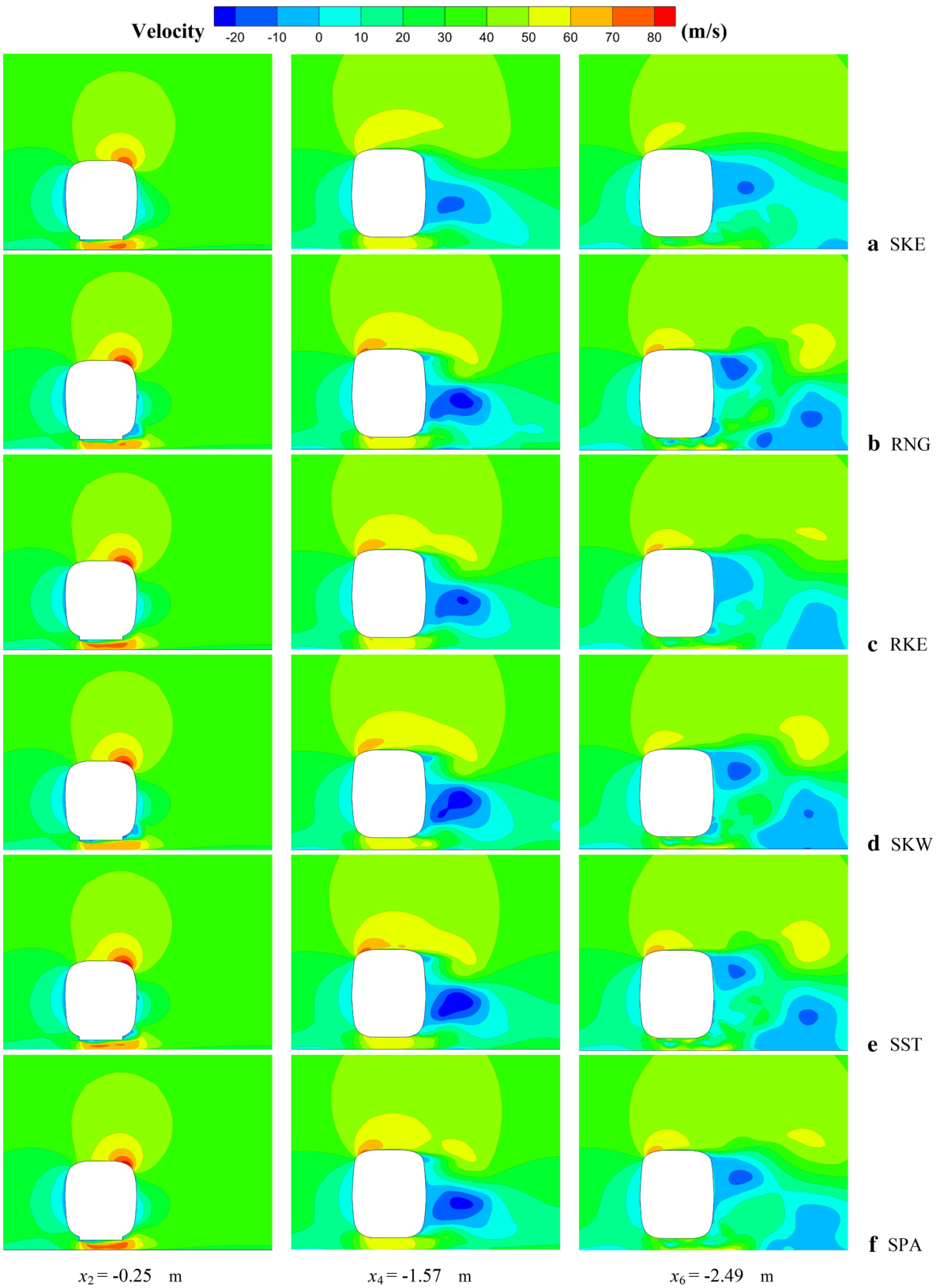

Figure 9 Velocity contour at different cross-sections

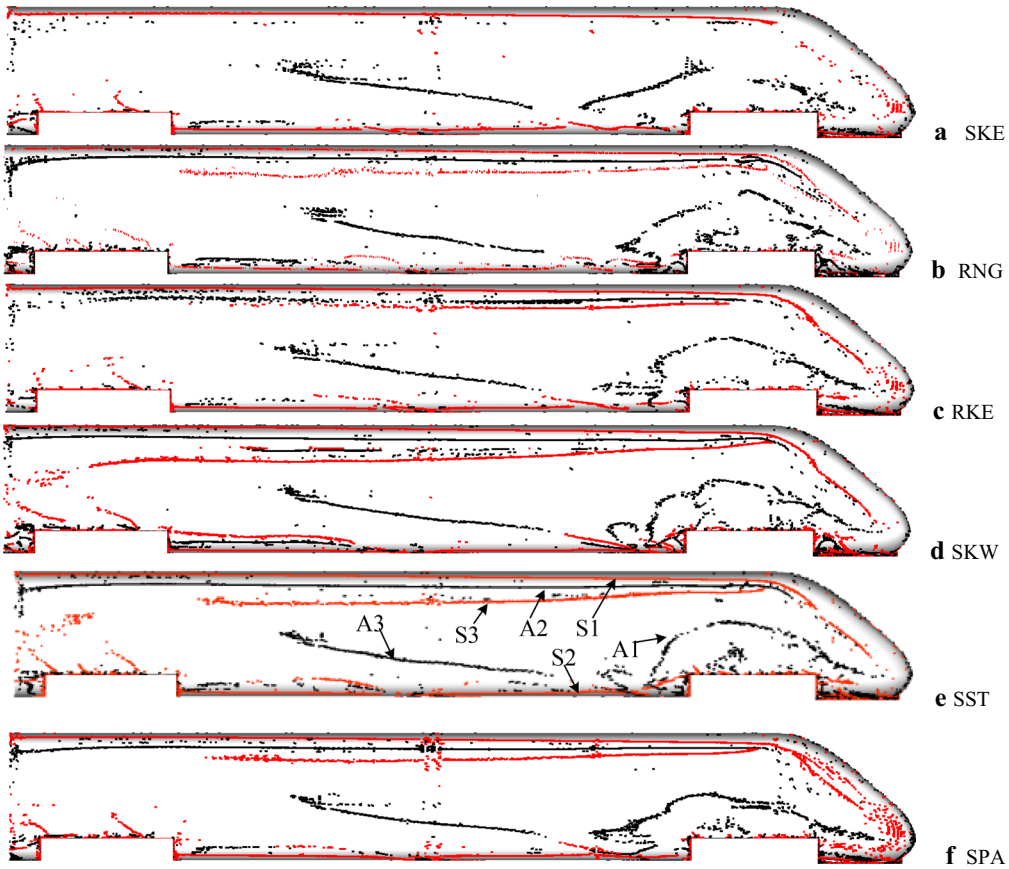

Figure 10 Surface flow on the leeward surface

at all cross-sections for different turbulence models are in a good agreement with the experimental results. The leeward surface also presents a reasonable match in pressure with the experimental data, indicating the rationality of the numerical method. As there are some differences in geometry between the numerical model and the experimental model, such as the bogie, the cylindrical support, and so on, a slight difference is observed on the bottom surface of train for the numerical results and experimental data.

At the cross-section $x_1 = -0.107$ m, the different turbulence models show a large difference at the bottom of the train due to the exist of the spoiler. It can be seen from Figure 13(b) that the bogie has a greater influence on the airflow underneath the train, and it shows a higher suction pressure than the experimental value. Due to the presence of the bogie, there is no experimental data for comparison at the cross-section $x_3 = -0.50$ m. Compared with the three cross-sections near the streamlined nose, the pressure on the latter three cross-sections are more intuitive than the experimental data due to the influence derived from the spoiler, the bogie and the cylindrical support. It can be seen from Figure 13(a) and (b) that the maximum negative pressure appears on the upper part of the leeward surface, and the maximum suction pressure appears on the windward surface of the streamlined part, indicating that the aerodynamic forces are concentrated in the streamlined part of the train. It can be seen that the pressure on the three cross-sections $x_2 = -0.25$ m, $x_3 = -0.50$ m and $x_4 = -1.57$ m are different in a certain for different turbulence models. These areas are relatively less affected by the spoiler, bogies and cylindrical supports. It can be seen from Figure 13(b) that SST turbulence model exhibits the largest suction pressure, which can be confirmed from the previous analysis of flow field. Therefore, SST turbulence model shows a more accurate prediction in the flow separation in the boundary layer. Meanwhile, the pressure obtained using SST turbulence model agrees well with the experimental one at the other cross-sections. At the non-streamlined cross-section ($x_3 = -0.50$ m), the suction pressure on the upper part of the leeward surface for SKE turbulence model is much lower than that of the other turbulence models, and SST and RNG turbulence models exhibit

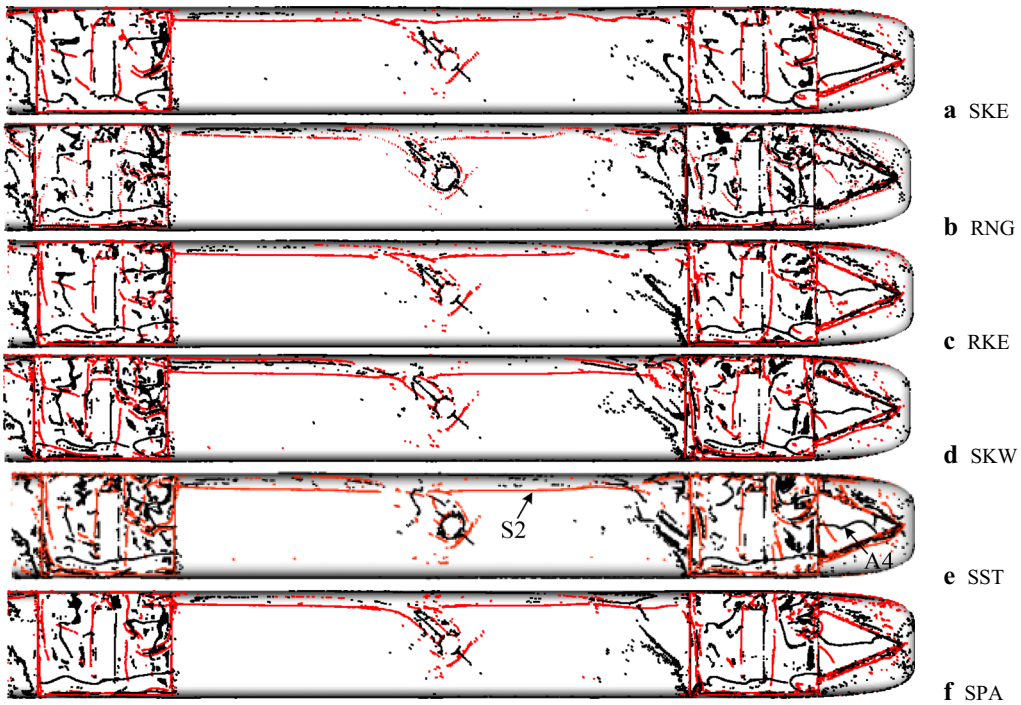

Figure 11 Surface flow on the bottom surface

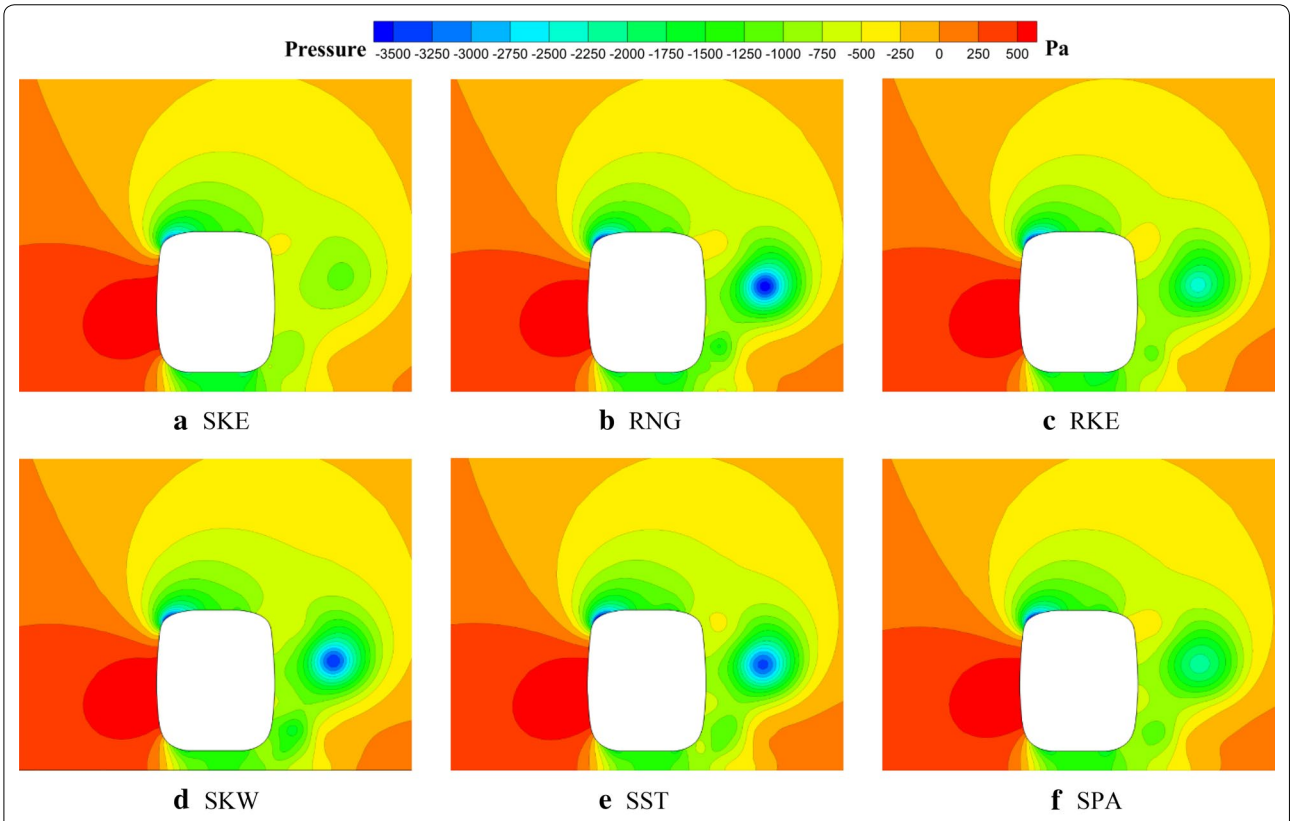

Figure 12 Pressure distribution at the cross-section $x_4 = -1.57$ m

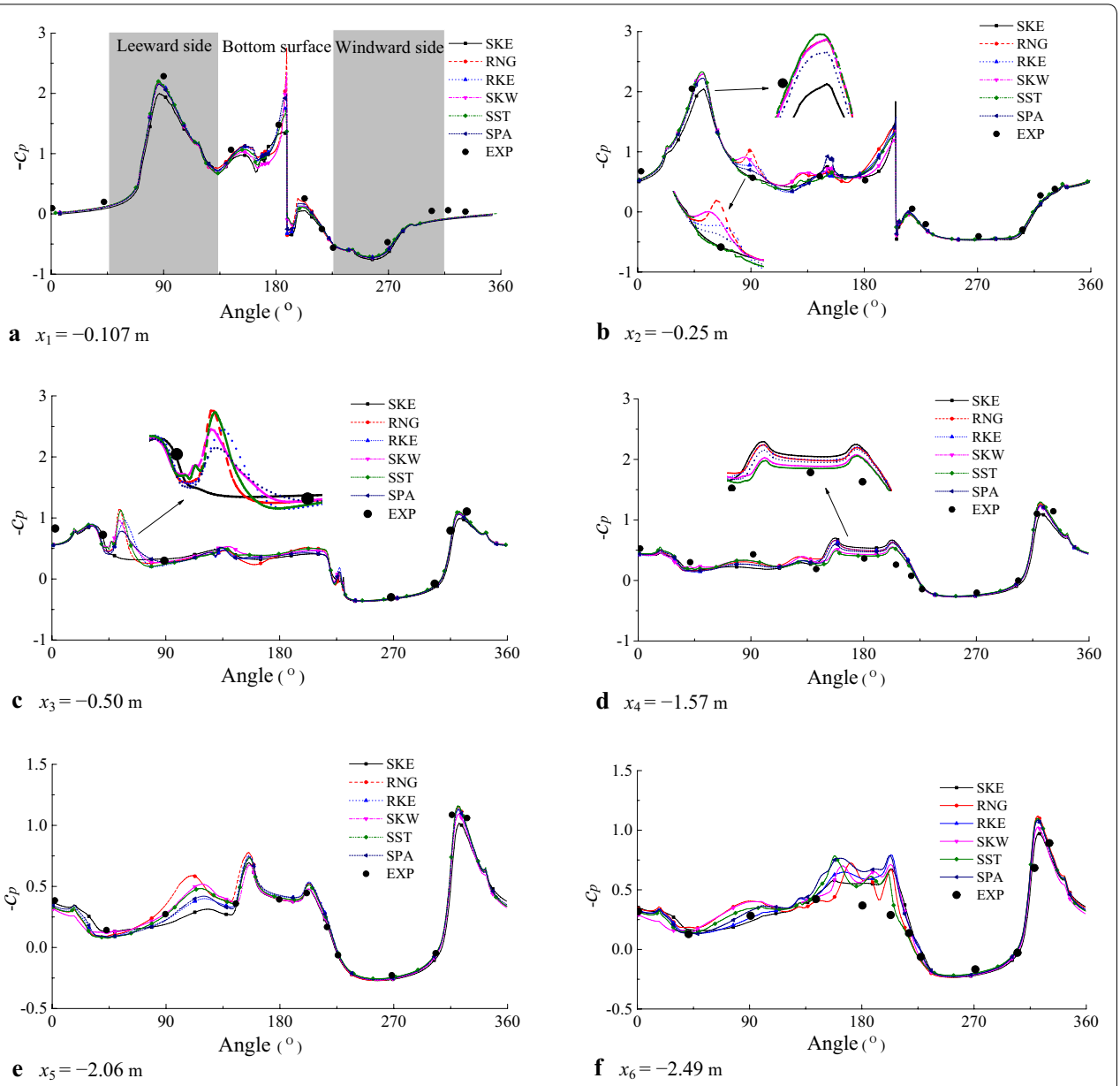

Figure 13 Comparison of pressure between numerical and experimental results

a higher suction pressure. On the bottom surface at the cross-section $x_4 = -1.57$ m, SST and SKW turbulence models agree well with the experimental values. Comprehensive comparison of the pressure on all cross-sections, SST turbulence model shows a better prediction on the surface pressure and also the flow field.

4.4 Aerodynamic Force

The difference in the side force coefficient c_s and lift force coefficient c_l between the numerical results and the experimental value [28] is studied. The results are given in Table 2. For the side force coefficient, the error is within 10% compared with the experimental value. Compared with the experiment results, the error for SST turbulence model is 0.5%, and for SKE turbulence model is 8.06%, followed by RNG with an error of 4.53%.

For the lift force coefficient, SST shows a more accurate result with an error of 21.8%, followed by RNG model, the error is 26.3%, and SKE predicts the worst. The deviation could be induced by a considerable geometric difference between the numerical and the experimental models. Some researchers have studied the aerodynamic

Table 2 Comparison of numerical and experimental values

Turbulence model	c_s	Relative error (%)	c_l	Relative error (%)
SKE	4.29	8.06	1.55	−36.2
RNG	4.15	4.53	1.79	−26.3
RKE	3.94	−0.76	1.54	−36.6
SKW	3.88	−2.27	1.68	−30.9
SST	3.99	0.50	1.90	−21.8
SPA	3.91	−1.51	1.55	−36.2
EXP	3.97	–	2.43	–

performance of ICE2 trains [13]. The relative error in the lift force coefficient between the numerical result and the experimental ones is from −31.1% to −47.6%. In this study, it provides a more accurate result with an error of −21.8%.

In the streamlined part of the head car, when the airflow transitions from the top of the train to the leeward surface, the airflow separates and a negative high-pressure zone is formed at the separation point. On the leeward surface at the cross-section $x_1 = -0.107$ m, the different negative pressure is generated using different turbulence models. The pressure predicted using SST is the largest, which results in the closest forces to the experimental ones. At the cross-section $x_2 = -0.25$ m, the pressure for SST turbulence model is also the largest, and that for SKE model is also the smallest, which matches the deviation. For the SKE turbulence model, the flow assumed is completely turbulent regardless of the role of molecular viscous, the viscous effect dominates the near wall of the train, and the turbulent development is not sufficient, and the calculation produces distortion. In the transition zone of the curved surface and the near-wall area of the surface, SKE is distorted by the low Reynolds number, and the pressure on the surface of the fitted body is small. It is shown in Table 2 that the SKE model shows the largest error, and SST model gives a minimum error. At the cross-section $x_4 = -1.57$ m, SST turbulence model gives the closest prediction in pressure on the bottom surface of the train, followed by SKW. Meanwhile, at the cross-section $x_6 = -2.49$ m, the pressure obtained using RNG and SST is close to the experimental one. It can be concluded from the above analysis that the SST and RNG models have better predictions in the lift force coefficient.

5 Conclusions

The accuracy of the numerical simulation of the external flow around trains by means of different turbulence models is analyzed with comparison to the wind tunnel experimental data. The results are as follows.

(1) In the numerical simulation of the external flow around trains subjected to crosswind, different turbulence models show quite different performances at specific regions. The pressure on the windward surface is quite similar for all turbulence models. Compared with the experimental results, the side force coefficient obtained using SST *k-ω* turbulence model is the closest to the experimental one, and the error is within 1%. The error of the side force coefficient for both standard *k-ε* and RNG *k-ε* models is large, and the error is large than 4%, the standard *k-ε* model shows the worst prediction in the side force coefficient. Meanwhile, SST *k-ω* model gives a relatively small error in the prediction of the lift force coefficient.

(2) The standard *k-ε* turbulence model is established for complete turbulence. As a high Reynolds number model, the calculation results in distortion in the near-wall region where viscous action dominates. The standard *k-ε* model is not suitable for surface curved flow and complex vortex flow. As a modification of the standard *k-ε* model, the Realizable *k-ε* model is a good simulation of the low Reynolds number flow in the near-wall region, and has the ability in the accurate prediction of the lift force coefficient, however, it fails to predict accurately in the side force coefficient. The standard *k-ω* and SST *k-ω* models are suitable for the low Reynolds number, and the separation prediction caused by the inverse pressure gradient is more accurate, however, the predicted separation region using the standard *k-ω* model is larger. SST *k-ω* model combines the advantages of the standard *k-ω* and standard *k-ε* models, and presents the closest results for both the lift and side forces among 6 turbulence model mentioned in this study.

Authors' Contributions

TL was in charge of the whole trial and wrote the manuscript; DQ assisted with the post process of the data and analysis; JZ revised the manuscript and gave some advices. All authors read and approved the final manuscript.

Authors' Information

Tian Li, born in 1984, is currently a Research Associate at *State Key Laboratory of Traction Power, Southwest Jiaotong University, China*. He received his doctor degree from *Southwest Jiaotong University, China*, in 2012. His research interests include train aerodynamics.

Deng Qin, born in 1996, is currently a master candidate at *State Key Laboratory of Traction Power, Southwest Jiaotong University, China*.

Jiye Zhang, born in 1965, is currently a professor at *State Key Laboratory of Traction Power, Southwest Jiaotong University, China*. He received his PhD degree from *Southwest Jiaotong University, China*, in 1998. His research interests include train aerodynamics, stability and control of complex systems.

Competing Interests
The authors declare that they have no competing interests.

Funding
Supported by National Natural Science Foundation of China (Grant No. 51605397), Sichuan Provincial Science and Technology Program of China (Grant No. 2019YJ0227), and Self-determined Project of State Key Laboratory of Traction Power (Grant No. 2019TPL_T02).

Received: 22 December 2018 Revised: 13 October 2019 Accepted: 14 October 2019
Published online: 24 October 2019

References

[1] N J Yan, X Z Chen, Y L Li. Assessment of overturning risk of high-speed trains in strong crosswinds using spectral analysis approach. *Journal of Wind Engineering and Industrial Aerodynamics*, 2018, 174: 103-118.
[2] T Li, M G Yu, J Y Zhang, et al. A Fast Equilibrium State Approach to Determine Interaction between stochastic crosswinds and High-speed Trains. *Journal of Wind Engineering and Industrial Aerodynamics*, 2015, 143: 91-104.
[3] M G Yu, J L Liu, D W Liu, et al. Investigation of aerodynamic effects on the high-speed train exposed to longitudinal and lateral wind velocities. *Journal of Fluids and Structures*, 2016, 61: 347-361.
[4] Y Ding, M Sterlings, C J Baker. An alternative approach to modelling train stability in high cross winds. *Proceedings of the Institution of Mechanical Engineers Part F-Journal of Rail and Rapid Transit*, 2008, 222(1): 85-97.
[5] C Baker. The flow around high speed trains. *Journal of Wind Engineering and Industrial Aerodynamics*, 2010, 98: 277-298.
[6] M Wang, X Z Li, J Xiao, et al. An experimental analysis of the aerodynamic characteristics of a high-speed train on a bridge under crosswinds. *Journal of Wind Engineering and Industrial Aerodynamics*, 2018, 177: 92-100.
[7] Z W Chen, T H Liu, Z H Jiang. Comparative analysis of the effect of different nose lengths on train aerodynamic performance under crosswind. *Journal of Fluids and Structures*, 2018, 78: 69-85.
[8] L Zhang, J Zhang, T Li, et al. A multi-objective aerodynamic optimization design of a high-speed train head under crosswinds. *Proceedings of the Institution of Mechanical Engineers Part F: Journal of Rail and Rapid Transit*, 2017, 232(3): 895-912.
[9] S Huang, H Hemida, M Yang. Numerical calculation of the slipstream generated by a crh2 high-speed train. *Proceedings of the Institution of Mechanical Engineers Part F: Journal of Rail and Rapid Transit*, 2016, 230(1): 103-116.
[10] F Dorigatti, M Sterling, C J Baker, et al. Crosswind effects on the stability of a model passenger train – a comparison of static and moving experiments. *Journal of Wind Engineering and Industrial Aerodynamics*, 2015, 138: 36–51.
[11] T Li, J Y Zhang, W H Zhang. A numerical approach to the interaction between airflow and a high-speed train subjected to crosswind. *Journal of Zhejiang University-Science A,* 2013, 14(7): 482-493.
[12] M G Yu, J Y Zhang, W H Zhang. Multi-objective optimization design method of the high-speed train head. *Journal of Zhejiang University-Science A*, 2013, 14(9): 631-641.
[13] B Diedrichs, M Sima, A Orellano, et al. Crosswind stability of a high-speed train on a high embankment. *Proceedings of the Institution of Mechanical Engineers Part F: Journal of Rail and Rapid Transit*, 2007, 221(2): 205-225.
[14] F Cheli, F Ripamonti, D Rocchi, et al. Aerodynamic behaviour investigation of the new EMUV250 train to cross wind. *Journal of Wind Engineering and Industrial Aerodynamics,* 2010, 98(4): 189-201.
[15] T Li, M Li, Z Wang, et al. Effect of the inter-car gap length on the aerodynamic characteristics of a high-speed train. *Proceedings of the Institution of Mechanical Engineers Part F-Journal of Rail and Rapid Transit*, 2019, 233(4): 448-465.
[16] B Diedrichs. Aerodynamic calculations of crosswind stability of a high-speed train using control volumes of arbitrary polyhedral shape. *BBAA VI International Colloquium on: Bluff Bodies Aerodynamics and Applications, Milano, Italy*, 2008.
[17] J A Morden, H Hemida, C J Baker. Comparison of RANS and detached-eddy simulation results to wind-tunnel data for the surface pressures upon a class 43 high-speed train. *Journal of Fluids Engineering-Transactions of the ASME*, 2015, 137(4): 041108.
[18] H Hemida, C J Baker. Large-eddy simulation of the flow around a freight wagon subjected to a crosswind. *Computers and Fluids*, 2010, 39(10): 1944-1956.
[19] H Hemida, S Krajnovic. Exploring flow structures around a simplified ICE2 train subjected to a 30 degrees side wind using LES. *Engineering Applications of Computational Fluid Mechanics*, 2009, 3(1): 28-41.
[20] S Krajnovic, P Ringqvist, K Nakade, et al. Large eddy simulation of the flow around a simplified train moving through a crosswind flow. *Journal of Wind Engineering and Industrial Aerodynamics*, 2012, 110: 86-99.
[21] S B Yao, Z X Sun, D L Guo, et al. Numerical study on wake characteristics of high-speed trains. *Acta Mechanica Sinica*, 2013, 29(6): 811-822.
[22] J Zhang, J J Li, H Tian, et al. Impact of ground and wheel boundary conditions on numerical simulation of the high-speed train aerodynamic performance. *Journal of Fluids and Structures*, 2016, 61: 249-261.
[23] C Fu, M Uddin, A C Robinson. Turbulence modelling effects on the CFD predictions of flow over a NASCAR Gen 6 racecar. *Journal of Wind Engineering and Industrial Aerodynamics*, 2018, 176: 98-111.
[24] F Gao, H D Wang, H Wang. Comparison of different turbulence models in simulating unsteady flow. *Procedia Engineering*, 2017, 205: 3970-3977.
[25] S B Wang, R B James, B David, et al. The performance of different turbulence models (URANS, SAS and DES) for predicting high-speed train slipstream. *Journal of Wind Engineering and Industrial Aerodynamics*, 2017, 165: 46-57.
[26] J Munoz-Paniagua, J García, B Lehugeur. Evaluation of RANS, SAS and IDDES models for the simulation of the flow around a high-speed train subjected to crosswind. *Journal of Wind Engineering and Industrial Aerodynamics*, 2017, 171: 50-66.
[27] H K Versteeg, W Malalsasekera. *An introduction to Computational Fluid Dynamics*. Edinburgh: Pearson Education Limited, 2007.
[28] A Orellano, M Schober. Aerodynamic performance of a typical high-speed train. *Proceedings of the 4th WSEAS International Conference on Fluid Mechanics and Aerodynamics*, Elounda, August 21-23, 2006.